Springer

Acta Mechanica Sinica

CrossMark click for updates

• RESEARCH PAPER •

Acta Mech. Sin., Vol. 41, 424560 (2025)
https://doi.org/10.1007/s10409-024-24560-x

Energy absorption and failure mechanisms of nacre-like structure under low/high-velocity impact loading: a numerical study

Weitao Gao[1], Zihao Wang[1*], Kefeng Peng[1], Kehong Wang[2,3], Qi Zhou[2,3], and Zhijun Zheng[1,4*]

[1] *CAS Key Laboratory of Mechanical Behavior and Design of Materials, Department of Modern Mechanics, University of Science and Technology of China, Hefei 230027, China;*
[2] *School of Materials Science and Engineering, Nanjing University of Science and Technology, Nanjing 210094, China;*
[3] *Key Laboratory of Controlled Arc Intelligent Additive Manufacturing Technology, Ministry of Industry and Information Technology, Nanjing University of Science and Technology, Nanjing 210094, China;*
[4] *The State Key Laboratory of Nonlinear Mechanics, Institute of Mechanics, Chinese Academy of Sciences, Beijing 100190, China*

Received September 26, 2024; accepted October 16, 2024; published online August 19, 2025

Nacre-like structures exhibit excellent mechanical properties under low-velocity impact, but the effectiveness of the nacre-like designs under high-velocity impact remains unclear. In this study, the process of a spherical projectile impacting on a nacre-like plate over a wide range of velocities is simulated using the finite element method. A three-dimensional finite element model is constructed and validated against the test data of the target perforation in terms of residual velocity and fracture morphology. The effects of impact velocity, interface strengths, and geometric sizes on the impact resistance capabilities are systematically investigated, and a dimensionless geometrical parameter is proposed to reveal the mechanism affecting the fracture toughness of nacre-like materials. It is found that the impact resistance of the nacre-like material gradually weakens with impact velocity increasing and is inferior to that of homogeneous plates under high-velocity impact. Moreover, the fracture toughness of nacre-like materials depends on the competition mechanism between interfacial enhancement and strength weakening at different impact velocities. These findings provide significant guidance on applying bio-inspired structures to design protective materials.

Nacre-like material, Impact resistance, Finite element model, Failure mechanism

Citation: W. Gao, Z. Wang, K. Peng, K. Wang, Q. Zhou, and Z. Zheng, Energy absorption and failure mechanisms of nacre-like structure under low/high-velocity impact loading: a numerical study, Acta Mech. Sin. **41**, 424560 (2025), https://doi.org/10.1007/s10409-024-24560-x

1. Introduction

Technological advancements and the expansion of human activities across diverse sectors have driven the escalating demand for impact-resistant structures. The applications in aerospace, automotive, construction, and medical equipment require materials and structures with superior impact resistance. For example, in aerospace, aircraft, and spacecraft must withstand impacts and vibrations experienced during flight, while in automotive applications, vehicle structures must protect passengers during collisions. Brittle materials, such as ceramics [1, 2], glass [3, 4], and concrete [5-7], are commonly used in lightweight impact-resistant structures because they offer excellent hardness relative to their density. These materials exhibit high stiffness and compressive strength but are prone to fracture or breakage in the tension state, thereby constraining their practical applications for high performance. Moreover, the elevated processing cost of these materials restricts their large-scale application.

Organisms have evolved unique microstructures with excellent mechanical properties after long-term natural selection, which can guide the design of impact-resistant structures. These distinctive microstructures have been demonstrated to exhibit superior mechanical properties in specific aspects [8-12]. The properties of biomimetic materials are

*Corresponding authors. E-mail addresses: hwangzi@ustc.edu.cn (Zihao Wang); zjzheng@ustc.edu.cn (Zhijun Zheng)

Executive Editor: Haoshen Chen

dominated by the material microstructure instead of only constituents, and the reasonable material distribution gives a more efficient use of the constituents, expanding the property space beyond that of bulk materials. Over the past several decades, many biomimetic protective structures have been developed by emulating natural composites, demonstrating superior mechanical properties to their homogeneous counterparts. The sea mollusk and mantis shrimp are renowned predator-prey pairs known for their unique structural bioarmor in protective design. The nacreous layer of mollusk shells comprises 95% Vol. brittle aragonite tablets (bricks) arranged in interlocked layers, with the remaining 5% Vol. being tough organic matter (mortar) between tablets, serving as an adhesive between these tablets [13]. This brick-mortar configuration facilitates energy dissipation mechanisms such as crack propagation along soft material interfaces [11,14,15] and sliding between layers [10], thereby enhancing the structural toughness under impact loading. Consequently, the claw of mantis shrimp can preserve the integrity of the structure during hammering due to its intricate microscale fibers with helical stacking, known as Bouligand structure [16]. This arrangement enables multilevel crack deflection [17,18], further promoting energy dissipation.

Despite biological composite structures exhibiting potential for impact resistance, they are not designed to endure higher-velocity impacts due to the limited attack capabilities of their natural predators [19]. The existing studies are about the bending strength, fracture toughness, energy absorption, and crack propagation of bio-inspired structures under quasi-static loads or low-velocity impacts. The research on their performance under high-velocity impact loads is relatively limited. However, the velocity spectrum of impacts is notably broad in real-world conditions, typically spanning approximately 10 m/s for vehicle collisions, 10^2 m/s to 10^3 m/s for ballistic impacts, and 10^3 m/s to 10^4 m/s for space debris impacts. The dynamic response of materials and structures under high-velocity impact differs significantly from that of low-velocity impact, involving factors such as stress wave effects, thermal effects, and high strain rate behavior of materials. Therefore, future research needs to continue optimizing and improving the performance of bio-inspired structures under low-velocity impacts while expanding their application research under high-velocity impact conditions to enhance their applicability and reliability in real-world engineering scenarios.

In this study, the dynamic toughening mechanism of the nacreous structure subjected to impacts ranging from low to high velocity is investigated. In Sect. 2, a 3D finite element model (FEM) of a nacre-like plate is constructed, and its accuracy is validated through existing experimental results. In Sect. 3, the mechanical responses of the nacre-like plate under projectile impact at varying velocities are presented. The impact resistance of the nacre-like plate under high-velocity impact loading is studied. Furthermore, the effects of impact velocity, interface strengths, and geometric parameters on the impact resistance and fracture mechanisms of the nacre-like structures are explored. Conclusions are presented in Sect. 4.

2. Finite element model

2.1 Nacre-like plate

Numerical simulations of a nacre-like plate impacted by a spherical projectile were established to analyze the failure mechanism of the nacreous structure using commercial finite element software ABAQUS/Explicit. In simulations, the square target (60 mm × 60 mm × 6 mm) was supported simply on a rigid frame, as illustrated in Fig. 1. The spherical projectile hit the center of the plate, and its diameter is 6.35 mm, the initial velocity is V_0, the mass is M, and the total kinetic energy is E_k. The projectile is regarded as a rigid body according to the results of a spherical projectile impacting a homogeneous glass plate [20]. The nacre-like plate is composed of regular hexagonal glass tablets (edge width L_c and thickness L_t) stacked staggered along the longitudinal direction, with a total number of layers of N_L, as depicted in Fig. 1. The deformation and damage were captured to evaluate the impact resistance performance of the nacre-like plate.

2.2 Constitutive model of brittle material

The brittle glass was used as the matrix material of the nacre-like plate to achieve a mechanical behavior close to that of aragonite in natural shells. A dynamic constitutive model [21,22] was used to describe the mechanical behavior of the brittle material, which comprises mainly an equation of state (EOS), a damage-based strength model, and the strain rate effect.

The EOS defines the polynomial relationship between hydrostatic pressure p and Euler volume strain μ, which can be written as

$$p = \begin{cases} K_1\mu, & \mu \le 0, \\ K_1\mu + K_2\mu^2 + K_3\mu^3, & \mu > 0, \end{cases} \tag{1}$$

where K_1, K_2, K_3 are the material constants determined from plate impact tests.

The strength model characterizes the relationship between yield strength σ_Y and hydrostatic pressure p, written as $\sigma_Y = Y(p)r_\theta$, where r_θ represents Lode effect [21], and Y

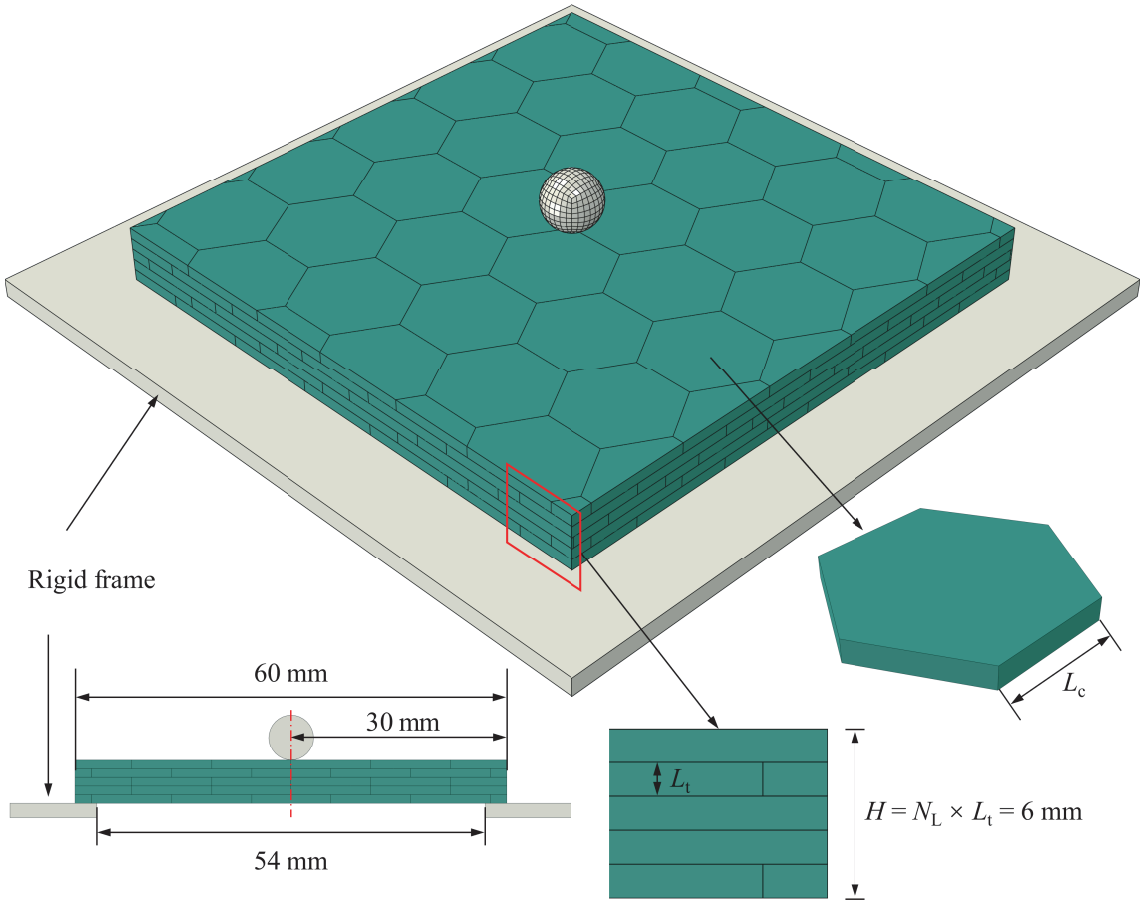

Figure 1 Schematic diagram of a spherical projectile impact on a nacre-like plate.

is expressed as

$$Y = \begin{cases} 3\left(f_{tt} + p\right), & p \le 0, \\ 3\left[f_{tt} + \left(1 - 3f_{tt}/f_{cc}\right)p\right], & 0 < p \le f_{cc}/3, \\ f_{cc} + Bf_c \tanh\left[\left(p - f_{cc}/3\right)/f_c\right], & p > f_{cc}/3, \end{cases} \tag{2}$$

where $f_{cc} = \eta_c f_c \psi_c$ and $f_{tt} = \eta_t f_t \psi_t$ are respective dynamic strengths of brittle materials in uniaxial compression and tension; f_c and f_t denote quasi-static uniaxial compressive and tensile strengths, respectively; η_c and η_t are shape functions which describe shear and tensile damage [21]. ψ_c and ψ_t are respective dynamic increase factors (DIF) due to strain rate effect only in uniaxial compression and tension, which can be written as [21, 23, 24]

$$\psi_c = \left(\psi_t - 1\right)\frac{f_t}{f_c} + 1, \tag{3}$$

and

$$\psi_t = \left(F_m - W_y\right)\tanh\left[S\left(\lg \dot{\varepsilon}^* - W_x\right)\right] + W_y, \tag{4}$$

where $\dot{\varepsilon}^* = \dot{\varepsilon}/\dot{\varepsilon}_0$ is the dimensionless strain rate, and $\dot{\varepsilon}_0$ is the reference strain rate usually taken to be $1.0\,\mathrm{s}^{-1}$; F_m, W_x, W_y, and S are constants determined from experimental tests.

The residual strength of the crushed ceramics is still high under the confining pressure. The residual yield surface for ceramics materials can be written as

$$Y_r = \begin{cases} 3p, & 0 < p \le f_r/3, \\ f_r + Bf_c \tanh\left[\left(p - f_r/3\right)/f_c\right], & p > f_r/3, \end{cases} \tag{5}$$

where $f_r = f_c r$ represents the residual strength under quasi-static uniaxial compression. Meanwhile, $f_c l$ corresponds to the initial yield strength. r and l are material constants.

The constitutive model was incorporated into the software ABAQUS by coding subroutine VUMAT to simulate the mechanical response of glass under impact load. In the constitutive model, the EOS parameters of glass are taken from Ref. [25]. The strength parameters were estimated by curve-fitting experimental data [26], as illustrated in Fig. 2. The strain rate effect parameters were obtained by fitting (Fig. 3) to the experimental data in Ref. [25]. The values of all the other parameters were estimated using the guidelines outlined in Ref. [22]. The main material parameters of the glass used in this

study are given in Table 1, and additional parameters follow with Refs. [21, 22].

2.3 Interface model

The cohesive zone model (CZM) was employed to describe the dynamic mechanical behavior of the adhesive layer between tablets. The CZM was widely used to simulate the adhesive layer bonding ceramics to metal or fiber [27]. The organic matter that acts as a binder in the nacreous structure makes up only about 5% of the total volume [13]. Hence, a cohesive contact method (without solid material) is adopted for numerical simulations. The traction-separation law describes the relationship between the cohesive nominal traction stress vector $\boldsymbol{T} = [t_\mathrm{n}, t_\mathrm{s}, t_\mathrm{t}]^\mathrm{T}$ and the corresponding separations $\boldsymbol{\delta} = [\delta_\mathrm{n}, \delta_\mathrm{s}, \delta_\mathrm{t}]^\mathrm{T}$, where the subscripts n, s, and t denote the normal and two tangential components, respectively. $\boldsymbol{K} = [K_\mathrm{n}, K_\mathrm{s}, K_\mathrm{t}]^\mathrm{T}$ is defined as the stiffness along the normal and tangential directions and satisfies $\boldsymbol{T} = (1-D)\boldsymbol{K\delta}$, where D is the damage variable. A simple bilinear traction-separation law is depicted in Fig. 4, where t_i^0 (i = n, s, t) represents the peak values of the traction stress when the separation is either purely normal to the interface or purely in the first or the second shear direction, respectively. Likewise, δ_i^0 (i = n, s, t) represents the values corresponding to the peak values of the traction. Damage begins to occur when the following criterion is satisfied:

$$\left\{\frac{\langle t_\mathrm{n}\rangle}{t_\mathrm{n}^0}\right\}^2 + \left\{\frac{t_\mathrm{s}}{t_\mathrm{s}^0}\right\}^2 + \left\{\frac{t_\mathrm{t}}{t_\mathrm{t}^0}\right\}^2 = 1, \tag{6}$$

where $\langle t_\mathrm{n}\rangle = t_\mathrm{n}$ if $t_\mathrm{n} > 0$ (tension) and $\langle t_\mathrm{n}\rangle = 0$ otherwise (compression), which signifies that a purely compressive stress state does not initiate damage. The Benzeggagh-Kenane fracture criterion [28] was adopted to describe damage evolution and failure of the interface. The fracture energy G^C required to cause failure in mixed-mode loading is defined as

$$G^\mathrm{C} = G_\mathrm{n}^\mathrm{C} + \left(G_\mathrm{s}^\mathrm{C} - G_\mathrm{n}^\mathrm{C}\right)\left(\frac{G_\mathrm{II}}{G_\mathrm{I}+G_\mathrm{II}}\right)^\eta, \tag{7}$$

where $G_\mathrm{I} = G_\mathrm{n}$, $G_\mathrm{II} = G_\mathrm{s}+G_\mathrm{t}$, and η is a cohesive property parameter; $G_\mathrm{n}, G_\mathrm{s}, G_\mathrm{t}$ denote the work done by the tractions and their conjugate separations in the normal, first and second-shear directions, respectively; the superscript C refers to the fracture energy required to cause failure in the corresponding

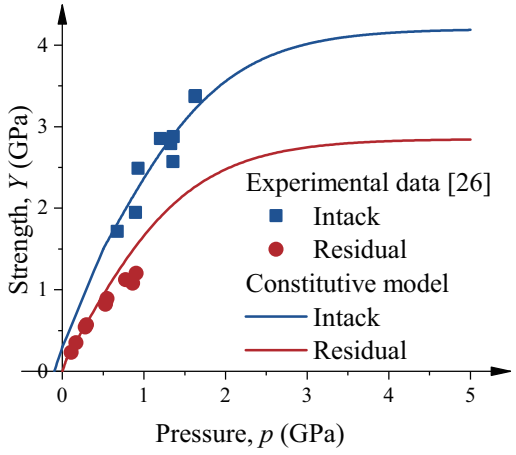

Figure 2 Strength model of the glass.

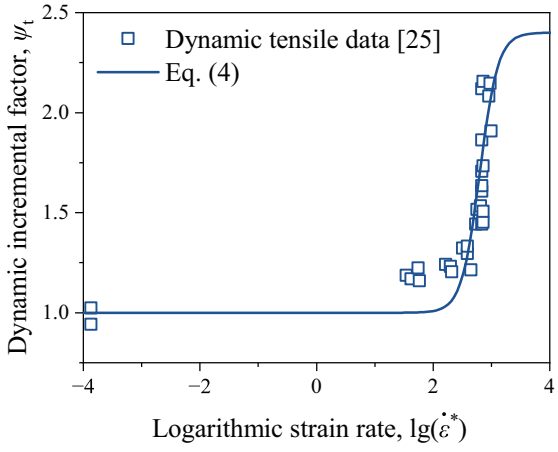

Figure 3 Strain rate effects.

Table 1 Main constitutive model parameters for glass [25, 26]

ρ (g/cm^3)	G (GPa)	f_c (MPa)	f_t (MPa)	K_1 (GPa)	K_2 (GPa)	K_3 (GPa)
2.53	26.9	1500	150	43.2	−67.2	153.2
B	l	r	F_m	W_x	W_y	S
1.5	0.8	0.05	2.4	2.8	1.7	3.2

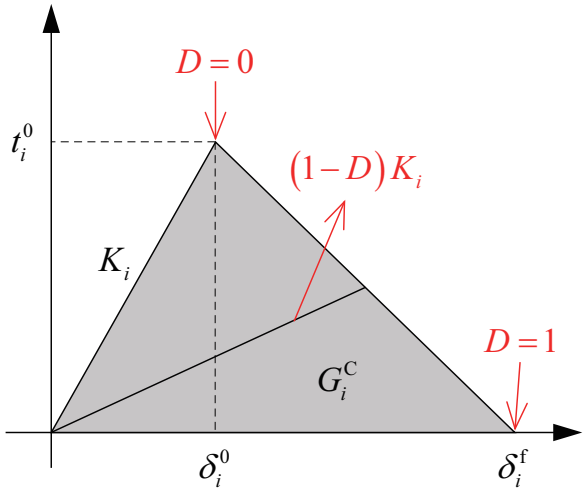

Figure 4 Bilinear traction-separation law (i = n, s, t).

directions. In this study, the mechanical behaviors along two shear directions are assumed to be the same ($K_s = K_t$, $t_s^0 = t_t^0$, and $G_s^C = G_t^C$), with specific parameters detailed in Table 2.

2.4 Validation of the finite element model

The reliability of the finite element model (FEM) was validated by comparing the numerical simulation and experimental results of the spherical projectile impacting homogeneous glass plate [20]. The process of a spherical projectile with a diameter of 6.35 mm impacting a square glass plate with a dimension of 100 mm × 100 mm × 12 mm was simulated. Crack propagation is a crucial mechanical behavior during the failure of brittle materials, which significantly impacts the failure zone and fragments of the material. Unfortunately, limited by computer computing capacity, it is difficult to simulate cracks accurately and efficiently due to the huge number of elements when the mesh size is close to the feature size of the crack. The local encryption of the mesh may alter the crack propagation pattern in the transition region from coarse to fine mesh. Therefore, a uniform mesh size of 0.4 mm ($\approx 2 \times 10^6$ solid elements) was ultimately selected, taking into account the mesh sensitivity and the computational time. The velocity of projectile ranges from 500 m/s to 800 m/s. The surroundings of the glass target plate are approximately free according to the experimental tests of Sathananthan et al. [20].

Table 2 Constitutive model parameters for interface

K_n (MPa/mm)	K_s (MPa/mm)	K_t (MPa/mm)	G_n^C (J/mm)
300	250	250	1.5
G_s^C (J/mm)	G_t^C (J/mm)	η	–
1.5	2.5	1.5	–

The deformation of the glass plate at the initial velocities of 500 m/s and 800 m/s are shown in Fig. 5. Under the projectile impact, cracks in plates mainly propagate in two forms: radial large cracks and circumferential small cracks. The distribution of the circumferential cracks is more extensive at the velocity of 500 m/s, while the size of the resulting fragments is smaller at 800 m/s. Figure 6 show the crack evolution of the plate during the impact process in experiments and numerical simulations. The overall distribution of the cracks obtained from the numerical simulations is consistent with the experimental results, but the number of cracks cannot be simulated accurately due to the mesh size of 0.4 mm, which is larger than the characteristic size of the crack. However, numerical simulations can accurately capture the velocity variation before and after the impact of the projectile (Fig. 7). The ballistic limit of 598 m/s can be approximated through the numerical simulation results, which closely align with 585 m/s predicted by the experimental results. When the projectile velocity surpasses this ballistic limit, the relative error between the numerical calculated residual velocity and the experimental results remains below 5%.

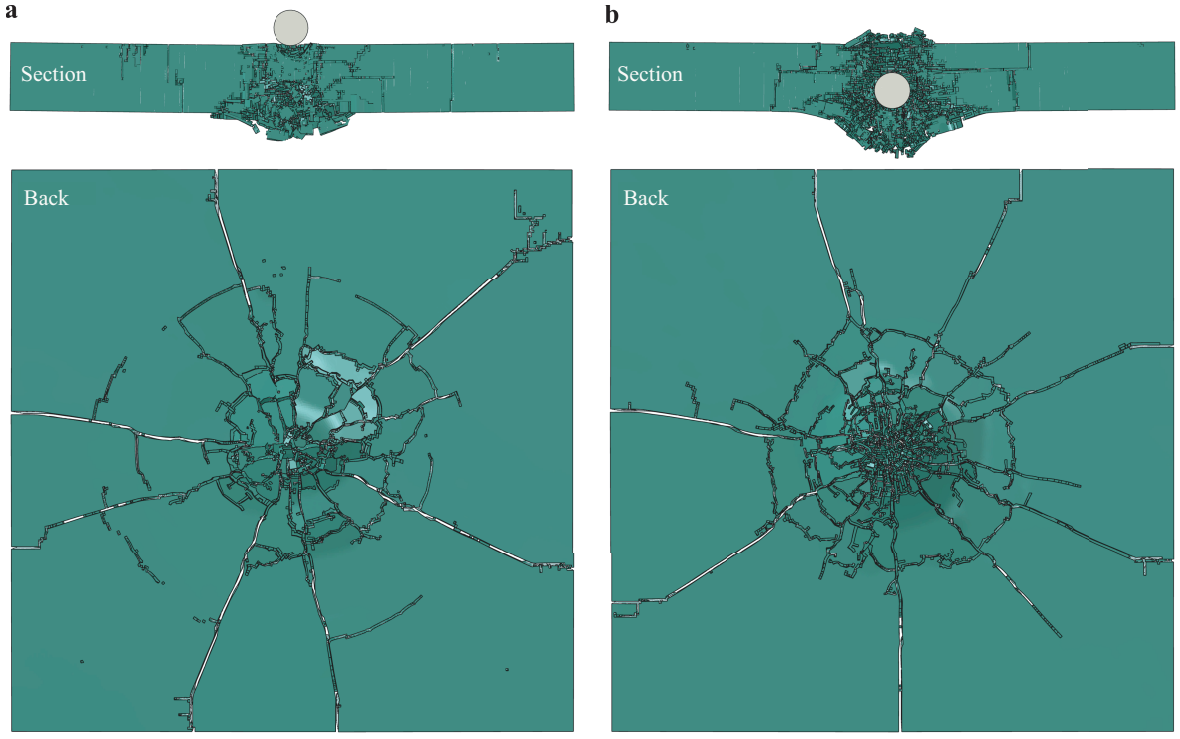

Figure 5 The deformation of the back of the glass plate after the projectile impact of 500 m/s **a** and 800 m/s **b**.

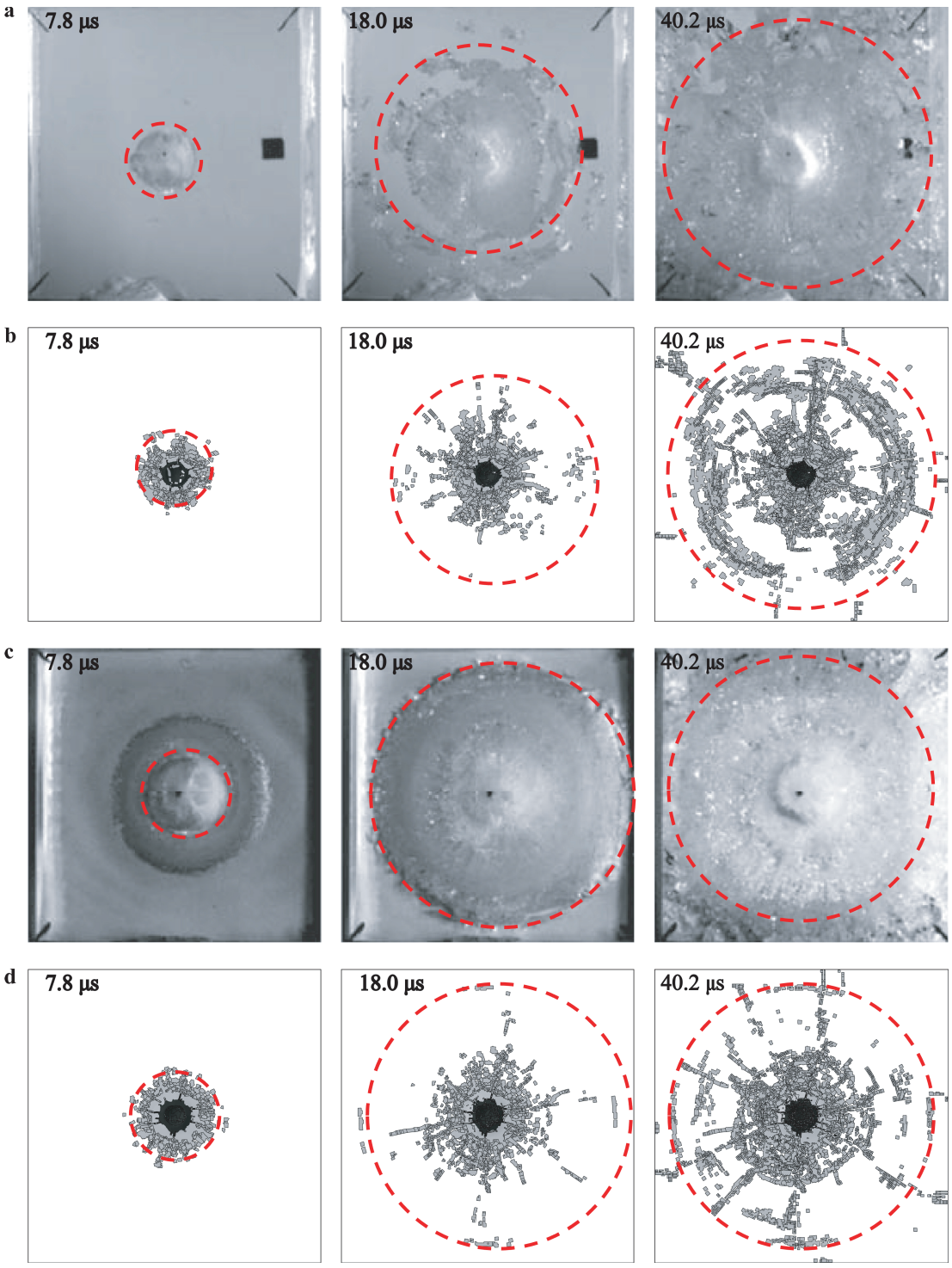

Figure 6 Comparison of experimental [20] (**a** and **c**) and simulated (**b** and **c**) results of crack and damage in the plate at the impact velocities of 500 m/s (**a** and **b**) and 800 m/s (**c** and **d**).

3. Results and discussion

3.1 Impact resistance of nacre-like plate at high velocity

Crack propagation patterns in the nacre-like plate and homogeneous plates at an initial velocity of 200 m/s are distinguished, as shown in Figs. 8 and 9. The dimensions of the nacre-like plate are $N_L = 5$ and $L_c = 6.4$ mm in the numerical simulation. A large number of short cracks appear in the circumferential direction first, followed by fewer large cracks along the radial direction in the front of the plate (Fig. 8a), while cracks propagate mainly along the radial direction in

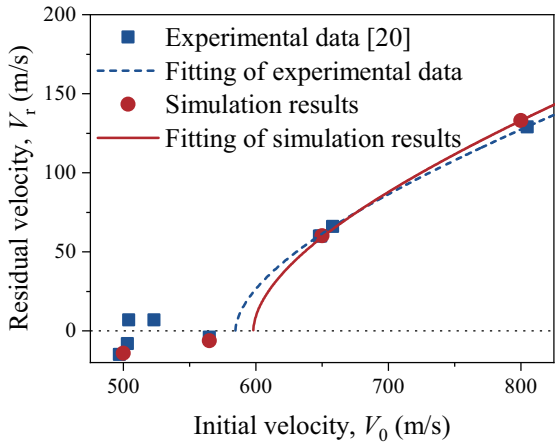

Figure 7 The residual velocity of the projectile after impact.

the back of the plate (Fig. 9a) when a homogeneous plate is subjected to a spherical projectile. However, for the nacre-like plate, a large number of short cracks are concentrated in a single hexagonal cell, and no large cracks propagate (Figs. 8b and 9b), thus the damage region in the nacre-like plate is much smaller than that in the homogeneous plate. These results indicate that stress propagation and crack extension will be blocked by the interfaces in a nacre-like plate.

The cross-sectional crack pattern of the nacre-like and homogeneous plates shows varying sensitivity to velocity, as shown in Figs. 10 and 11. The typical conical failure pattern is observed in both nacre-like and homogeneous plates subjected to a spherical projectile, a phenomenon also noted in brittle target [29,30]. The failure zone of the nacre-like plate exhibited a conical shape at an impact velocity of 100 m/s and 200 m/s, and the cater in the back decreases with impact velocity increasing. In contrast, the homogeneous plate displays a conical crack pattern at an impact velocity of 200 m/s, but a large dominated crack occurs in the cross-section at 100 m/s due to no penetration in the target. The perforation of a homogeneous plate was also observed in experimental tests [20], but at a higher impact velocity (> 500 m/s). This suggests that the impact velocity of the failure pattern transition is lower for the nacre-like plate compared to the homogeneous plate.

The energy absorption curves of the nacre-like plate with the impact velocity of 200 m/s are shown in Fig. 12. Due to the presence of the hourglass, the total energy of the system may increase during the impact process, but the increase can be ignored, ensuring the reliability of the obtained results. Spherical projectiles with different initial velocities were launched against both the nacre-like and homogeneous plates and the residual velocities are illustrated in Fig. 13. The ballistic limit for the nacre-like plate is determined to be

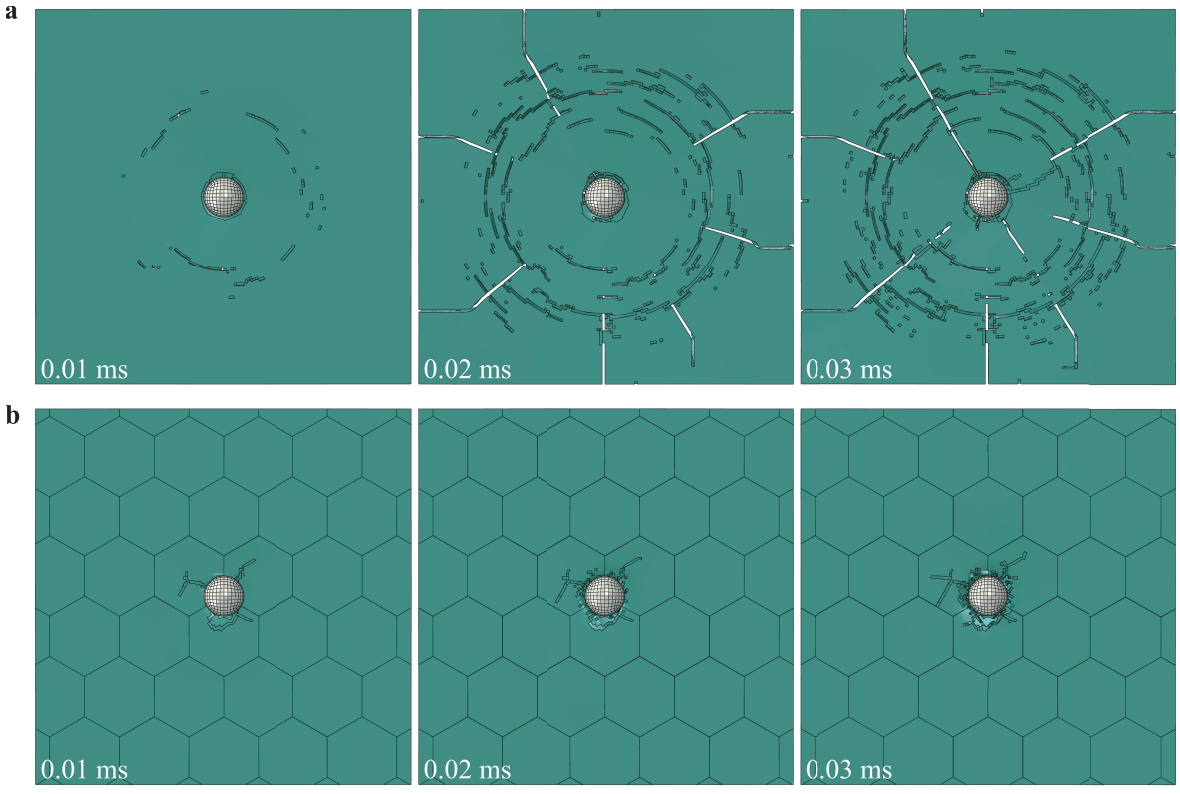

Figure 8 Crack propagation on the front of the homogeneous **a** and nacre-like **b** plate with V_0 = 200 m/s.

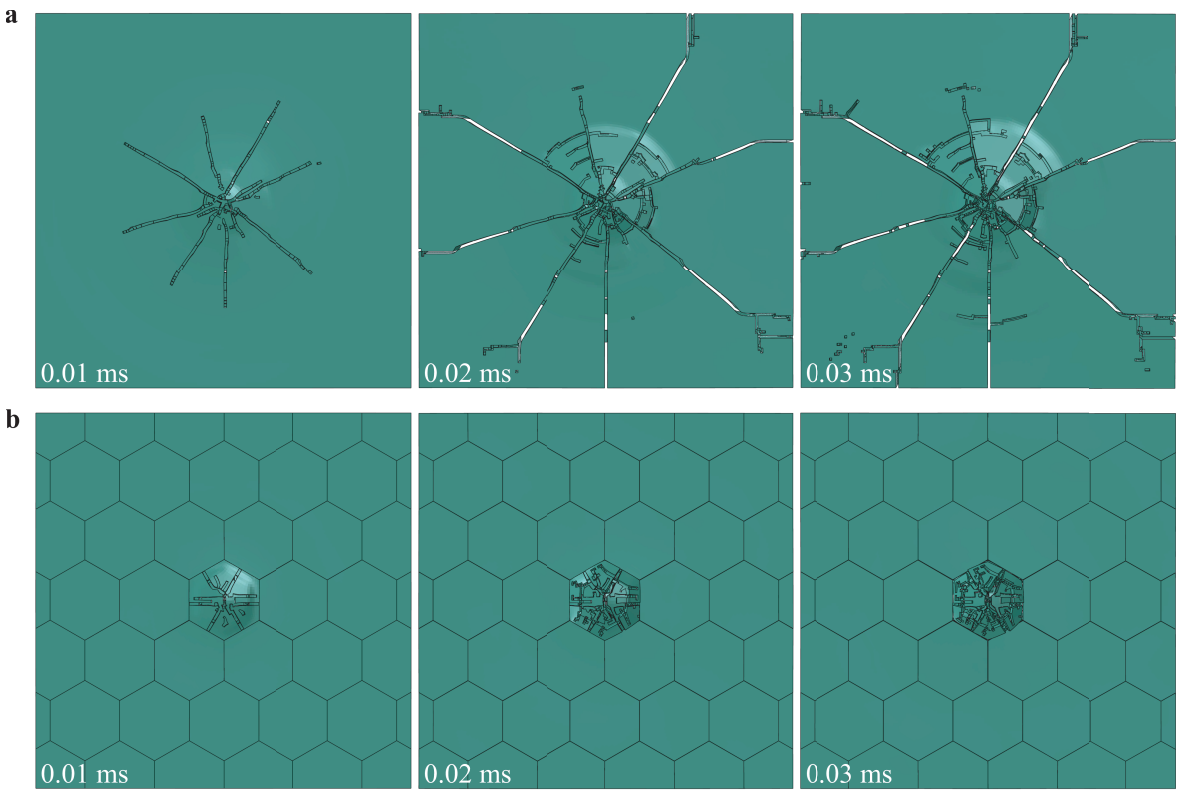

Figure 9 Crack propagation on the back of the homogeneous **a** and nacre-like **b** plate with V_0 = 200 m/s.

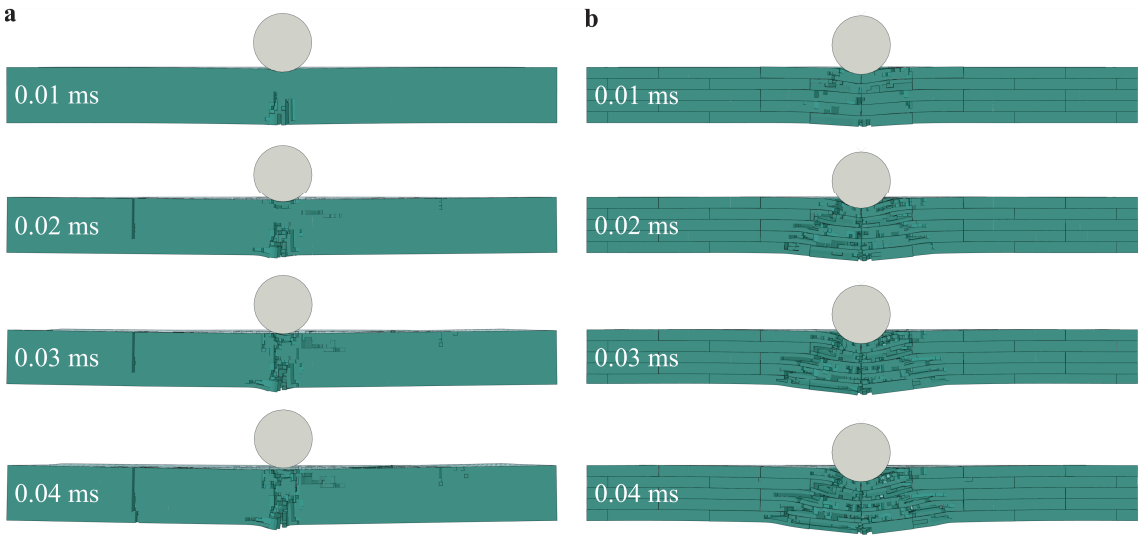

Figure 10 The section view of the deformation of the homogeneous **a** and nacre-like **b** plate with V_0 = 100 m/s.

97.6 m/s, a value lower than that of the homogeneous plate (136.8 m/s). Besides, it can also be observed that the residual velocity of the projectile is higher for the nacre-like plate at different impact velocities, which indicates a poorer impact resistance performance. These findings above suggest that the nacre-like plate does not enhance the protective efficacy at impact velocities exceeding 100 m/s.

3.2 Effects of impact velocity on the impact resistance

The impact resistance performance of the nacre-like plate may be affected by the impact velocity. Under quasi-static tests [31,32] and low-velocity impact [33,34], the efficacy of nacre-like structures in enhancing toughness has been substantiated. These results demonstrate a significant improve-

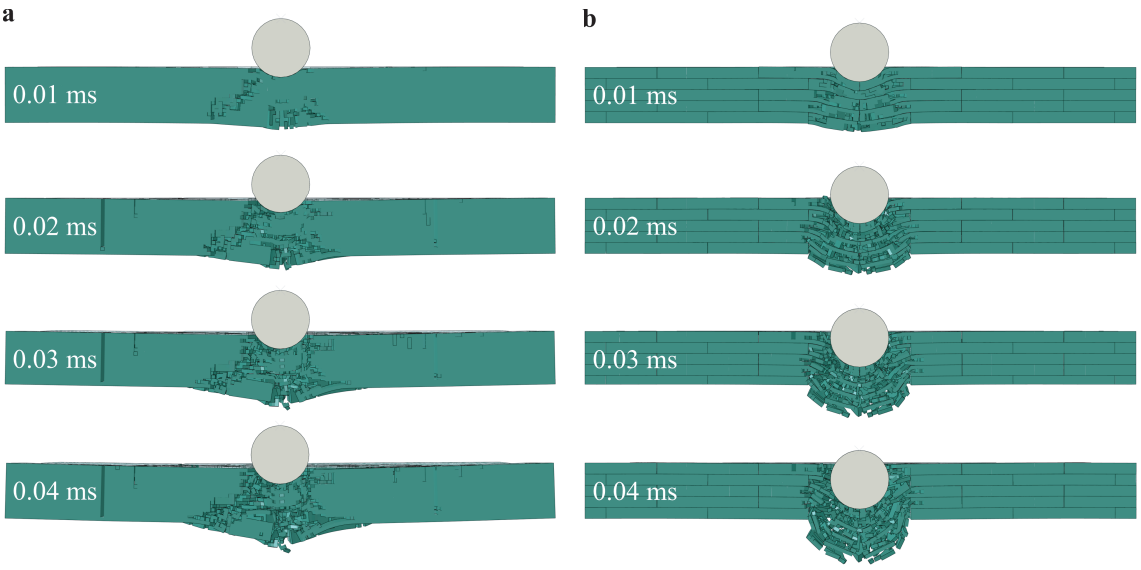

Figure 11 The section view of the deformation of the homogeneous **a** and nacre-like **b** plate with V_0 = 200 m/s.

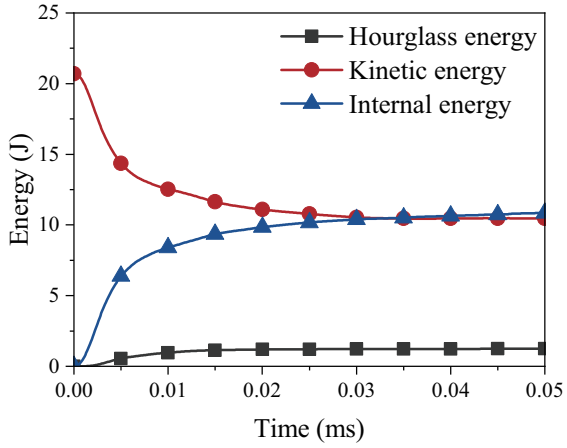

Figure 12 Energy absorption curves of the nacre-like plate with the impact velocity of 200 m/s.

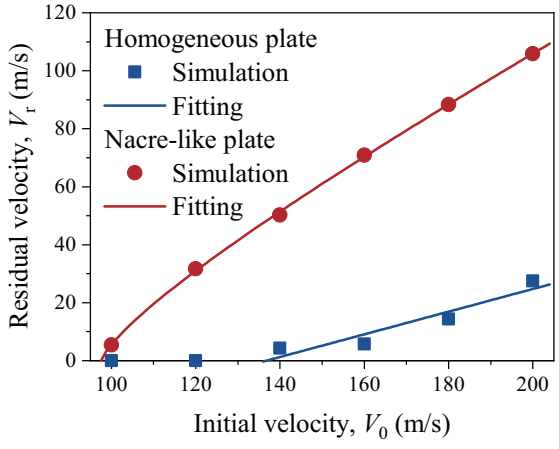

Figure 13 Residual velocity of the projectile with different initial velocities after impact.

ment compared to a homogeneous plate. While under high-velocity impact, the nacre-like plate does not enhance the protective efficacy. This discrepancy may arise from the variance in the mass of the impactor. In reality, the mass of an impactor for high-velocity impact is typically small, e.g., projectile impacting from a gun, whereas it is generally large for low-velocity impact, e.g., vehicle collisions. The mass of the projectile can be implicitly determined by the initial impact velocity V_0 and kinetic energy, denoted as E_k. The resistance of the nacre-like plate to impact was assessed under conditions of varying projectile velocities, all maintaining the same kinetic energy by manipulating the density of the projectile material rather than volume to avoid dimension mismatch between the projectile and the plate.

The deformation patterns observed in a plate subjected to a projectile impact at a velocity of 10 m/s differed significantly from those observed under high-velocity impacts, applicable to both homogeneous and nacre-like plates, as shown in Fig. 14. For a homogeneous plate, the cracks stop propagation along the toroidal direction, and there is a reduction in the number of radial cracks compared to the deformation depicted in Fig. 9a. A pronounced longitudinal deflection of the plate was noted, culminating in the collapse of the entire structure, as compared to the section deformation depicted in Fig. 11a. For the nacre-like plate, distinct radial cracks were observed on the rear surface of the plate. Additionally, the dimensions of the fragments within the fractured region area increased significantly (see Figs. 11b and 14b).

The impact resistance of the plate was assessed by calculating the absorbed energy, which represents the difference between the initial and final kinetic energies of the projectile. When V_0 = 200 m/s, the absorbed energy of the nacre-

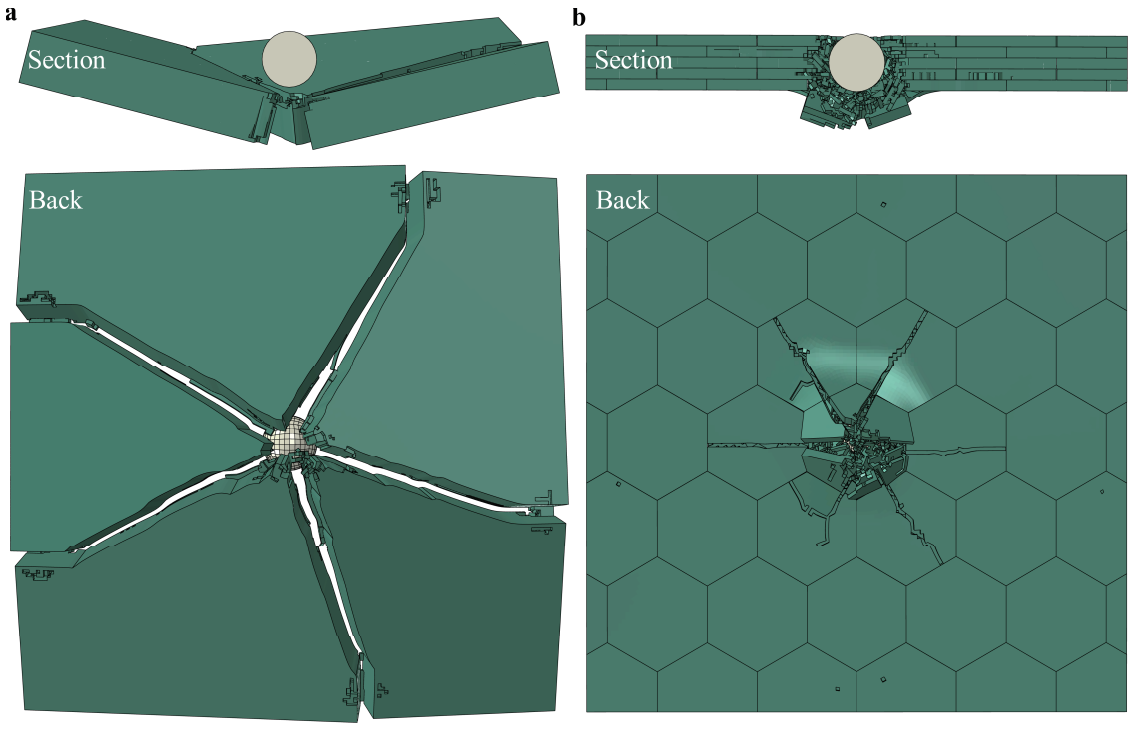

Figure 14 Deformation of the homogeneous **a** and nacre-like **b** plate with V_0 = 10 m/s and E_k = 5.17 J.

like plate is 14.74 J, which is lower than that of the homogeneous plate (20.51 J). However, when the velocity is reduced to 10 m/s, the absorbed energy of the nacre-like plate equals to 3.41 J, surpassing that of the homogeneous plate (1.68 J). This finding agrees with the results of the literature regarding the high toughness of the nacre-like plate compared to homogeneous plates at low-velocity impacts [33, 34]. Based on the analysis above, it is evident that the impact velocity of the projectile also influences the toughening capability of the nacre-like plate.

Comparing the history of the resistance force exerted on the projectile, it is evident that the nacre-like plate markedly extends the impact duration at lower velocities. This leads to superior energy absorption compared to the homogeneous plate despite its reduced resistance force. At an impact velocity of 10 m/s, the peak resistance force of the nacre-like plate is merely 20% of that of the homogeneous plate. However, the impact duration increases from 0.09 ms to 0.6 ms, as depicted in Fig. 15. During the impact process, the crack propagation path within a nacre-like plate is altered to extend solely along pre-designed paths (interfaces). The interfaces present in the plane impede the radial propagation of the crack, which limits the size of the failure region. The staggered stacking design of hexagonal tablets offers structural support, preventing the material adjacent to the projectile from being ejected in a plug-like manner. These factors collectively prevent the abrupt collapse of brittle materials, leading to a marked increase in the duration of impact. When the impact velocity is 200 m/s, the peak resistance force experienced by the projectile is about 50% of that of the homogeneous plate, but the duration of the impact is close to that of the homogeneous plate (about 0.06 ms), leading to a reduced energy absorption capacity. This suggests that the interface is unable to react to the impact of the projectile in such a short time. Notably, the rate at which stress is transferred between the interfaces is significantly slower than the speed of stress waves within a homogeneous plate. This results in a smaller failure area for the nacre-like plate, as illustrated in Fig. 11.

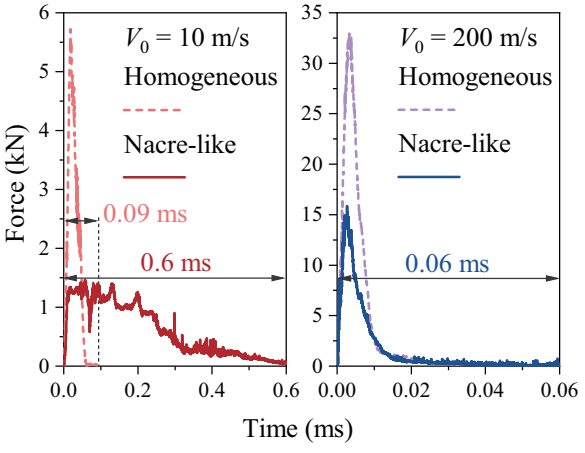

Figure 15 Resistance exerted on the projectile impacting a homogeneous and nacre-like plate at the velocities of 10 m/s and 200 m/s.

It becomes evident that under high-velocity impact loading, structural design plays a limited role, with the performance of the matrix material being more critical.

Figure 16 illustrates the energy absorption ratio E_a of the plate at varying impact velocities V_0, with E_k of 5.17 J, 11.64 J, 20.70 J and 46.57 J (equal to that of the projectile with the velocity of 100 m/s, 150 m/s, 200 m/s and 300 m/s and the density of 7850 kg/m^3), respectively. The results indicate that as the kinetic energy of the projectile remains constant, the value of E_a increases with V_0. The magnitude of E_a for the nacre-like plate is notably larger at a relatively low velocity. However, once the velocity of the projectile reaches a sufficient level, the E_a of the homogeneous plate surpasses that of the nacre-like plate. From the force-displacement curve in Fig. 15, we can infer that as the impact velocity decreases, the duration of the impact process increases. This longer impact duration dissipates more kinetic energy of the projectile, offsetting the negative impact of reduced resistance. When these two effects balance each other out, the corresponding impact speed is defined as the critical velocity. Then, the critical velocity can be obtained by the intersection of curves in Fig. 16. It is found that the critical velocity decreases as the projectile kinetic energy increases, as detailed in Fig. 17. When E_k falls below 10 J, V_c experiences a swift decay. However, as E_k exceeds 10 J, V_c declines very slowly in alignment with the rise in E_k. For a specified mass (M) and initial velocity (V_0) of the impactor striking both the nacre-like plate and the homogeneous plate, Fig. 18 illustrates which plate has greater impact resistance, and an approximate boundary line is delineated. The lower left region signifies that the nacre-like plate exhibits superior resistance, and the upper right indicates that the homogeneous plate is much greater. The results also indicate that when the impact velocity of the projectile is reduced to the order of 10 m/s, the nacre-like plate consistently exhibits superior anti-impact capabilities.

3.3 Effects of the interface strengths

The interface, a prevalent feature in biocomposites, is an efficient energy dissipation structure. The strength of the interface significantly influences the propagation of cracks within it, with tensile and shear strength emerging as crucial factors [35]. The numerical simulations of a nacre-like plate subjected to a spherical projectile were conducted with different t_s and t_n in equal proportions (t_n/t_s = 0.6). The failure separation displacement of the interface remained constant (δ_n = 0.2 mm, δ_s = 0.4 mm). The crack distributions observed in the nacre-like and homogeneous plates are similar when t_s reaches 1600 MPa (see Figs. 8, 9, 14 and 19). At low impact velocities, only radial cracks emerge, which results in the overall collapse of the nacre-like target. The phenomenon is distinguished from that observed in Fig. 14b (t_s = 25 MPa) where the damage zone is approximately 1 to 2 hexagonal cell. At elevated impact velocities, the nacre-like plate exhibits circumferential cracks in conjunction with the radial crack, as depicted in Fig. 8a, which can not occur at low interface strength, as shown in Figs. 8b and 9b. In conclusion, the dynamic mechanical behavior of the nacre-like plate under impact load progressively aligns with that of a homogeneous plate with increasing interface strength.

The energy absorption ratio E_a varies with interface strength, as illustrated in Fig. 20. The energy absorption ratio of the nacre-like plate decreases at low impact velocity; nevertheless, that increases at high impact velocity with the increase of interface strength, which will converge towards that of the homogeneous plate (black line in Fig. 20) when

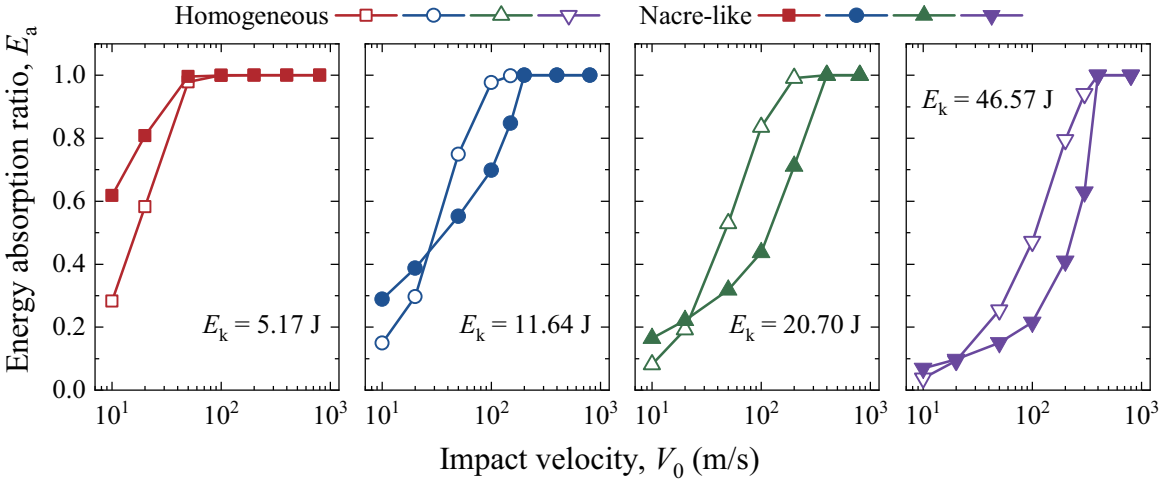

Figure 16 Energy absorption ratio of the nacre-like plate at different impact velocities and energies.

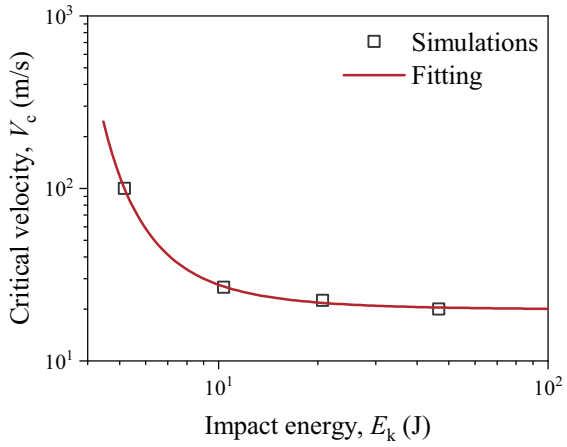

Figure 17 The critical velocity of the nacre-like plate under different impact energies.

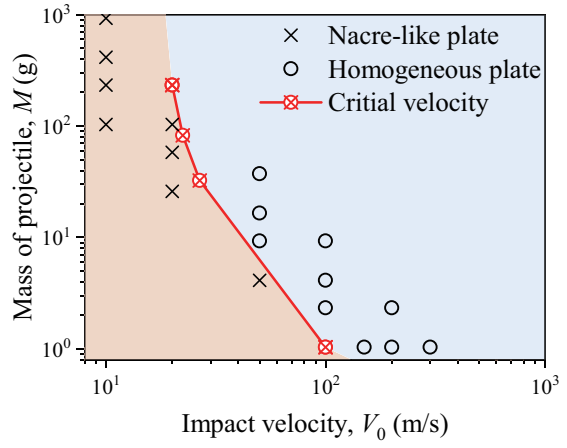

Figure 18 Phase diagram showing the optimal choice of homogeneous/nacre-like plates based on different masses and velocities of the projectile.

it approaches infinite. The critical velocity (V_c) of the nacre-like plate demonstrates insensitivity to interface strength (see Fig. 21). In other words, the weaker the interface, the better at low impact velocity, while a stronger interface is preferable at high impact velocity.

3.4 Effects of the geometric dimension of the hexagonal cell

The energy absorption ratios of the nacre-like plates with cell sizes L_c of 2.4 mm, 3.6 mm, 4.8 mm, 6.4 mm and 10.8 mm subjected to projectile impacts are shown in Fig. 22. The results indicate that at an impact velocity of 10 m/s, the energy absorption ratio decreases slightly from 0.25 to 0.17 as L_c escalates from 2.4 mm to 10.8 mm. However, at a relatively high impact velocity, the alterations in the energy absorption ratio are relatively insignificant, with variations of less than 3.5% across different L_c values. Thus, the energy absorption ratio is insensitive to the cell sizes.

The effects of the number of layers N_L of the nacre-like plates on the energy absorption ratio were also analyzed, and the results of the nacre-like plates with N_L of 1, 3, 5, and 15 were displayed in Fig. 23. In particular, $N_L = 1$ represents the homogeneous plate. It is observed that for the plates with different N_L, the energy absorption ratio exhibits significant variations and demonstrates distinct patterns under both low and high impact velocities. For plates with less than 5 layers, the energy absorption ratio experiences a slight increase at low impact velocities as the number of layers increases. Conversely, at high impact velocity, this ratio significantly decreases. However, for plates with more than 5 layers, the energy absorption ratio consistently increases with the number of layers. The results also indicate that only the nacre-like plate, with low impact velocities (10 m/s and 20 m/s), exhibits a higher energy absorption ratio compared to the homogeneous plate. This further suggests that the nacre-like structure does not confer an advantage at high velocities.

To further explore the intrinsic relationship between the energy absorption ratio of a nacre-like plate and the geometric dimensions of its unit cell, a dimensionless number termed α as the "interface area density" (IAD) was introduced. This factor represents the relative proportion of the total area of all material interfaces within the nacre-like plate to the cross-sectional area. The IAD includes two components: the intra-layer IAD (denoted as α_1) and the inter-layer IAD (denoted as α_2). Given that L_c can be inferred that IAD for a single layer equates to that of the triangle region in Fig. 24, which is expressed as $2L_t/\left(\sqrt{3}L_c\right)$, thus α_1 can be determined to be $\alpha_1 = 2N_L L_t/\left(\sqrt{3}L_c\right) = 2H/\left(\sqrt{3}L_c\right)$. When the nacre-like plate comprises N_L layers, the inter-layer IAD (α_2) is determined as $N_L - 1$. Consequently, the relationship between α and the geometric parameters of the nacre-like plate can be expressed as

$$\alpha = \alpha_1 + \alpha_2 = \frac{2H}{\sqrt{3}L_c} + N_L - 1. \tag{8}$$

Upon reorganizing the resultant data, we derived the E_a-α curves, which depict the relationship between the energy absorption ratio of the nacre-like plate and the IAD at different impact velocities, as illustrated in Fig. 25. The trend of the curve aligns closely with the results presented in Fig. 23. This is attributed to the fact that L_c employed in the numerical simulation is relatively large, which results in the effect of α_1 having a significantly less effect than α_2. This observation also explains the insignificant effect of L_c on the energy absorption ratio, as seen in Fig. 22. It is interesting to note that the energy absorption ratio increases at low impact velocity ($V_0 \leq 20$ m/s), first decreases, and then increases at

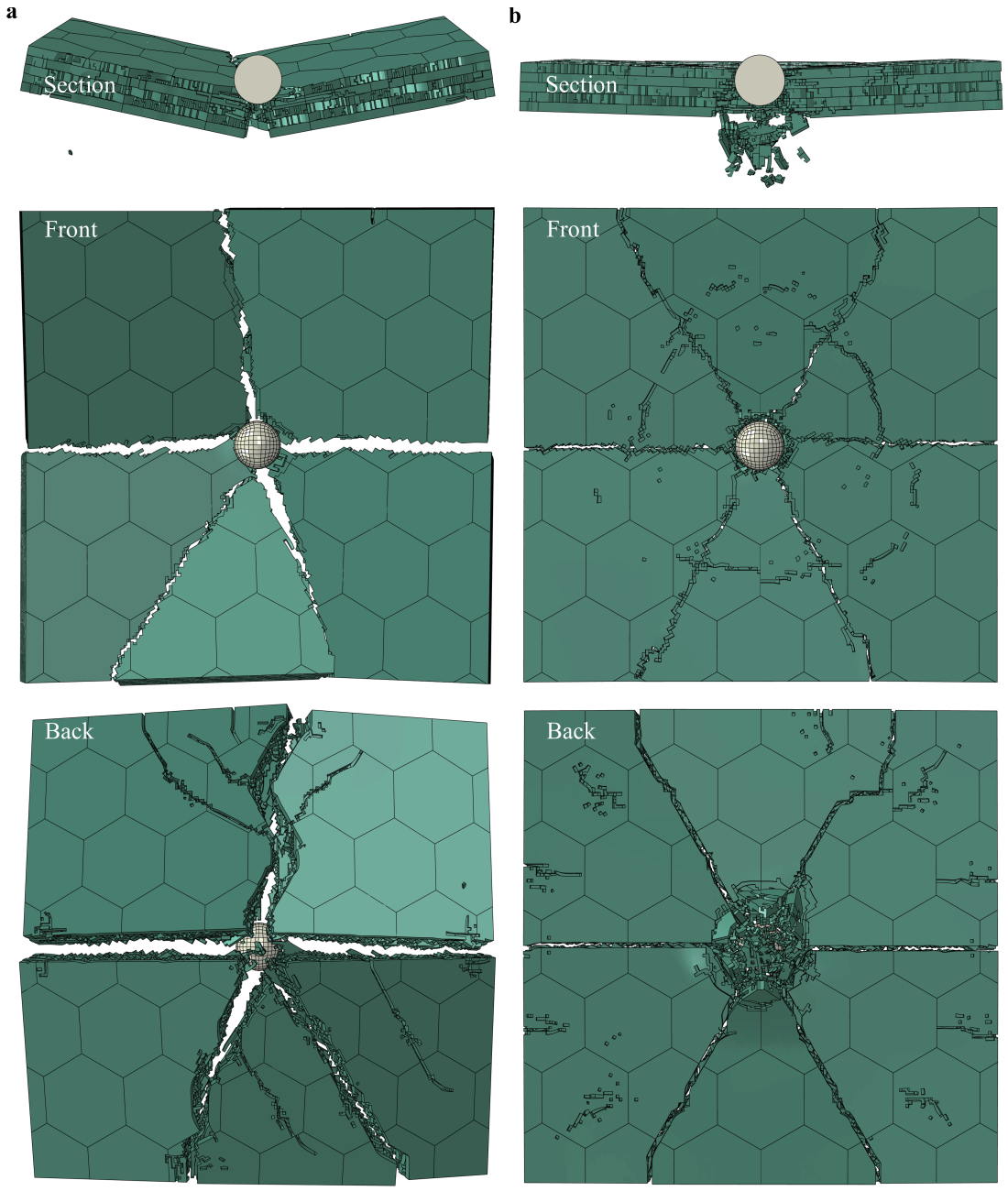

Figure 19 The deformation of the nacre-like plate at the impact velocity of 10 m/s **a** and 200 m/s **b** with t_s = 1600 MPa.

high impact velocity ($V_0 \geq 50$ m/s) with α increasing. This phenomenon indicates that the factors affecting the fracture toughness of nacre-like materials are not singular, and a competitive mechanism exists.

The resistance to a projectile of a target depends on the material strength and impact velocity [36,37]. Given that the density of the target plate and the velocity of the projectile remain constant, the resistance encountered by the projectile is contingent upon the material strength of the target plate. A projectile striking a sufficiently thick ceramic-like material at high velocities results in a conical region ahead of the projectile, as shown in Fig. 11a. This region experiences elevated confining pressure, which substantially increases material strength. In contrast, the presence of the interface in the nacre-like plate affects or even prevents the formation of the conical zone. The contour of hydrostatic pressure within the target plate (Fig. 26) during initial penetration reveals that the peak hydrostatic pressure within the nacre-like plate is merely 50% of that observed in the homogeneous plate, which is very aligned the results in Fig. 15. Much lower hydrostatic pressure corresponds to smaller material strength, called strength-weakening. At low impact velocities, inter-

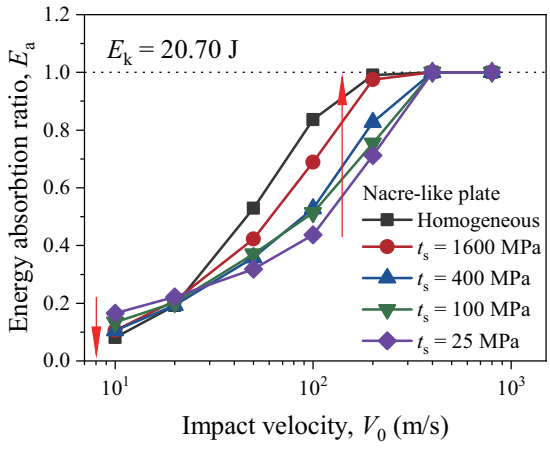

Figure 20 Energy absorption ratio of the nacre-like plate with varying interface strength.

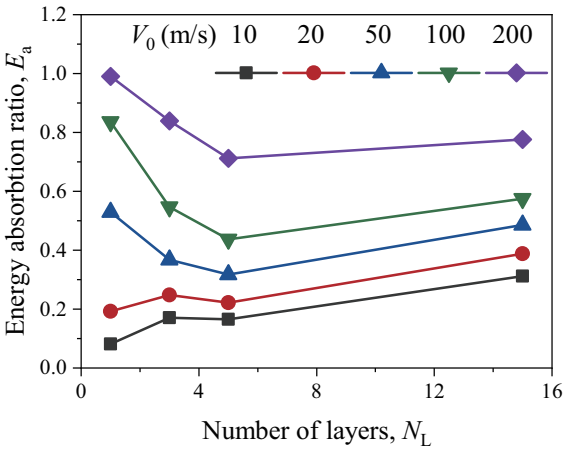

Figure 23 The effects of N_L on energy absorption ratio at different impact velocities (L_c = 6.4 mm except when N_L = 1).

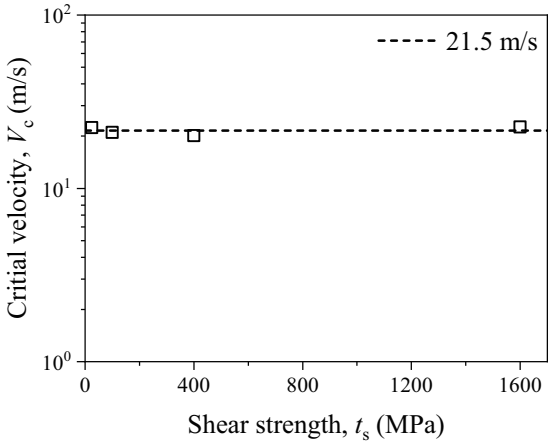

Figure 21 The effect of the interface strength on the critical velocity of the nacre-like plate.

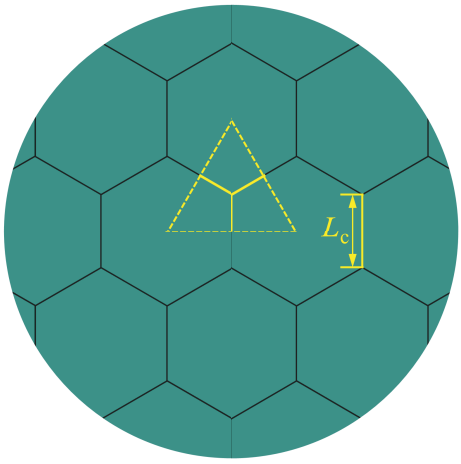

Figure 24 Schematic diagram of interface area density.

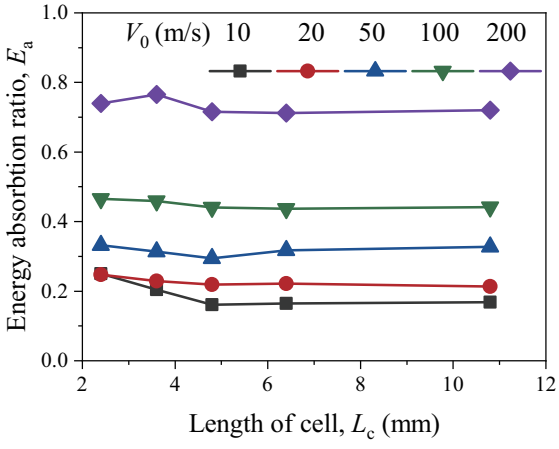

Figure 22 The effects of L_c on energy absorption ratio at different impact velocities (N_L = 5).

faces increase the duration of impact and offer an additional energy dissipation by crack propagation between them, rendering the nacre-like plate more impact-resistant. The feature could be called interface-enhancement, but its significance diminishes at high impact velocities.

Based on the analysis presented, the energy absorption ratio of the nacre-like plate can be expressed as $E_a = E_1 + E_2$. Here, E_1 denotes the portion toughened by the interface, while E_2 pertains to the impact velocity. As observed in Fig. 25, it is hypothesized that E_1 varies linearly with α, represented as $E_1 = k\alpha$. The velocity-dependent term comprises two components: one component represents the enhancement in energy absorption as the impact velocity increases (denoted as $g_1(V_0)$), as shown in Fig. 16. This enhancement arises because a higher impact velocity results in a lower projectile mass for a fixed impact energy, allowing the same resistance force to impart larger deceleration. The second component represents the reduction in energy absorption due to

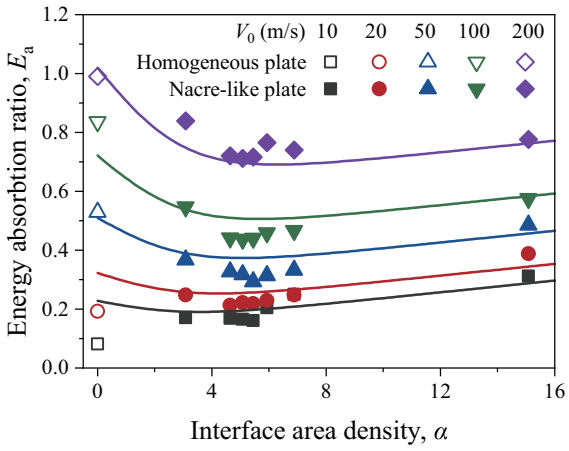

Figure 25 The effects of the IAD on energy absorption ratio.

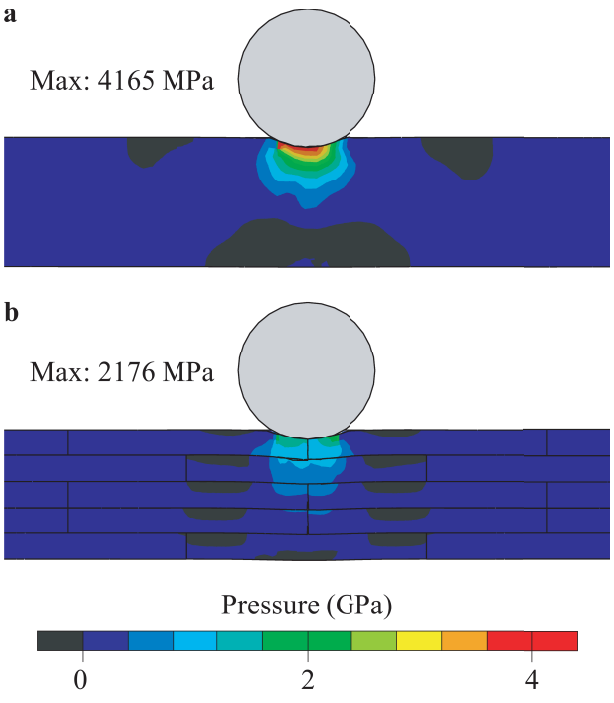

Figure 26 Pressure contour of the homogeneous **a** and nacre-like **b** plate at the time of 2.5 μs with V_0 = 200 m/s.

the diminished dynamic strength of the materials, denoted as $-g_2 \cdot h(\alpha)$. Here, g_2 is a function of the impact velocity, and $h(\alpha)$ increases with the rise in α. Assuming $g_1 = g_2 = g$, we can write $E_a = k\alpha + g(V_0)\,[1 - h(\alpha)]$. The final equation derived from this analysis is fitted as follows:

$$E_a = k\alpha + a\sqrt{\frac{V_0}{V_s}}\,[1 - b \cdot \tanh(c\alpha)]\,, \tag{9}$$

where k = 0.01, a = 1.02, b = 0.40, and c = 0.31; V_s represents standard velocity (200 m/s here, the velocity corresponding to E_k = 20.70 J and the projectile density of 7850 kg/m^3), as shown in Fig. 25.

When the value of V_0 is small, resulting in a very small V_0/V_s and $E_a \approx k\alpha + a\sqrt{V_0/V_s}$, it suggests that the interface-enhancement predominates at lower impact velocities. A larger α implies a greater interface, which can dissipate more kinetic energy of the projectile. This is confirmed by the curves for V_0 = 10 m/s and 20 m/s in Fig. 25. However, as impact velocity increases, the V_0/V_s enlarges, making the value of $ab\sqrt{V_0/V_s}\tanh(c\alpha)$ non-negligible. Consequently, strength weakening begins to dominate. It is evident from the characteristics of $\tanh(c\alpha)$ that as α increases, E_a initially decreases until α reaches a sufficient value, at which point $E_a \approx k\alpha + a(1-b)\sqrt{V_0/V_s}$. This is in agreement with Fig. 25, where E_a increases linearly with α for large values of α.

4. Conclusions

This study employs the finite element method to simulate the dynamic mechanical behavior of nacre-like plates subjected to projectile impact, thereby validating the efficacy of these structures under various impact velocities. Furthermore, the effects of impact velocity, interface strengths, and geometric sizes on the impact resistance performance and mechanisms were investigated. Our study suggests that:

- The plate with a nacre-like structure shows excellent resistance to low-velocity impacts but does not provide any advantage over a homogeneous plate under high-velocity impacts.
- There is a critical velocity describing the transition of fracture toughness from enhancement to weakening in nacre-like structures. This transition is attributed to the prolongation of the impact process at low impact velocities. Additionally, the critical velocity decreases rapidly as projectile impact energy increases, eventually stabilizing to the value of about 20 m/s in this study.
- The influence of the strength of interfaces in the nacre-like plate on impact resistance is different at different impact velocities. For low-velocity impact, the weak interface is instrumental in energy absorption. The strong interface is preferable for high-velocity impact.
- The competition of the interface-enhancement and strength-weakening of the nacre-like structure controls the impact resistance of the plate. The weakening effect of strength-weakening at low impact velocity is insignificant compared to the enhanced effect of the interface-enhancement, but becomes obvious at high impact velocity, leading to a substantial decrease in impact resistance compared to the homogeneous plate.

Conflict of interest *On behalf of all authors, the corresponding author states that there is no conflict of interest.*

Author contributions *Weitao Gao conducted a research and investigation process and wrote an original draft. Zihao Wang and Kefeng Peng helped organize the manuscript. Kehong Wang, Qi Zhou, and Zhijun Zheng provided ideas. Zhijun Zheng designed the methodology, revised and edited the final version, and provided funding support.*

Acknowledgements *This work was supported by the National Natural Science Foundation of China (Grant No. 12425210). We acknowledge the computer time provided by the Supercomputing Center of University of Science and Technology of China.*

1 C. E. Anderson Jr, and B. L. Morris, The ballistic performance of confined Al_2O_3 ceramic tiles, Int. J. Impact Eng. **12**, 167 (1992).
2 A. B. Dresch, J. Venturini, S. Arcaro, O. R. K. Montedo, C. P. Bergmann, Ballistic ceramics and analysis of their mechanical properties for armour applications: A review, Ceram. Int. **47**, 8743 (2021).
3 T. Benitez, S. Y. Gómez, A. P. N. de Oliveira, N. Travitzky, and D. Hotza, Transparent ceramic and glass-ceramic materials for armor applications, Ceram. Int. **43**, 13031 (2017).
4 L. S. Gallo, M. O. C. Villas Boas, A. C. M. Rodrigues, F. C. L. Melo, and E. D. Zanotto, Transparent glass-ceramics for ballistic protection: Materials and challenges, J. Mater. Res. Tech. **8**, 3357 (2019).
5 A. Rajput, and M. A. Iqbal, Impact behavior of plain, reinforced and prestressed concrete targets, Mater. Des. **114**, 459 (2017).
6 J. Feng, W. Sun, L. Wang, L. Chen, S. Xue, and W. Li, Terminal ballistic and static impactive loading on thick concrete target, Constr. Build. Mater. **251**, 118899 (2020).
7 R. A. Perkins, C. J. Duncan, D. Johnson, T. W. Stone, J. A. Sherburn, M. Chandler, R. D. Moser, B. Paliwal, R. K. Prabhu, and Y. Hammi, Assessment of a high strength concrete using experimental and numerical methodologies for high strain rate ballistic impacts, Int. J. Impact Eng. **178**, 104598 (2023).
8 J. D. Currey, Hierarchies in biomineral structures, Science **309**, 253 (2005).
9 H. Peterlik, P. Roschger, K. Klaushofer, and P. Fratzl, From brittle to ductile fracture of bone, Nat. Mater **5**, 52 (2006).
10 F. Barthelat, H. Tang, P. Zavattieri, C. Li, and H. Espinosa, On the mechanics of mother-of-pearl: A key feature in the material hierarchical structure, J. Mech. Phys. Solids **55**, 306 (2007).
11 L. T. Kuhn-Spearing, H. Kessler, E. Chateau, R. Ballarini, A. H. Heuer, and S. M. Spearing, Fracture mechanisms of the Strombus gigas conch shell: Implications for the design of brittle laminates, J. Mater. Sci. **31**, 6583 (1996).
12 J. C. Weaver, G. W. Milliron, A. Miserez, K. Evans-Lutterodt, S. Herrera, I. Gallana, W. J. Mershon, B. Swanson, P. Zavattieri, E. DiMasi, and D. Kisailus, The stomatopod dactyl club: A formidable damage-tolerant biological hammer, Science **336**, 1275 (2012).
13 H. D. Espinosa, J. E. Rim, F. Barthelat, and M. J. Buehler, Merger of structure and material in nacre and bone—Perspectives on de novo biomimetic materials, Prog. Mater. Sci. **54**, 1059 (2009).
14 S. Kamat, H. Kessler, R. Ballarini, M. Nassirou, and A. H. Heuer, Fracture mechanisms of the *Strombus gigas* conch shell: II-micromechanics analyses of multiple cracking and large-scale crack bridging, Acta Mater. **52**, 2395 (2004).
15 X. Y. Chan, C. Chua, S. Tan, and H. Le Ferrand, Energy dissipation in composites with hybrid nacre-like helicoidal microstructures, Compos. Part B-Eng. **232**, 109608 (2022).
16 Y. Bouligand, Twisted fibrous arrangements in biological materials and cholesteric mesophases, Tissue Cell **4**, 189 (1972).
17 K. Wu, Z. Song, S. Zhang, Y. Ni, S. Cai, X. Gong, L. He, and S. H. Yu, Discontinuous fibrous Bouligand architecture enabling formidable fracture resistance with crack orientation insensitivity, Proc. Natl. Acad. Sci. USA **117**, 15465 (2020).
18 S. M. Wen, S. M. Chen, W. Gao, Z. Zheng, J. Z. Bao, C. Cui, S. Liu, H. L. Gao, and S. H. Yu, Biomimetic gradient Bouligand structure enhances impact resistance of ceramic-polymer composites, Adv. Mater. **35**, 2211175 (2023).
19 W. Huang, D. Restrepo, J. Y. Jung, F. Y. Su, Z. Liu, R. O. Ritchie, J. McKittrick, P. Zavattieri, and D. Kisailus, Multiscale toughening mechanisms in biological materials and bioinspired designs, Adv. Mater. **31**, 1901561 (2019).
20 P. Sathananthan, A. Sirois, D. Singh, and D. Cronin, Sphere on tile ballistic impact experiment to characterize the response of soda lime glass, Int. J. Impact Eng. **133**, 103321 (2019).
21 H. Xu, and H. M. Wen, A computational constitutive model for concrete subjected to dynamic loadings, Int. J. Impact Eng. **91**, 116 (2016).
22 R. T. Tang, L. Y. Xu, H. M. Weng, Z. H. Wang, A macroscopic dynamic constitutive model for ceramic materials, Chin. J. High Press. Phys. **34**, 89 (2020).
23 H. Xu, and H. M. Wen, Semi-empirical equations for the dynamic strength enhancement of concrete-like materials, Int. J. Impact Eng. **60**, 76 (2013).
24 Z. H. Wang, H. M. Wen, H. Zheng, and J. S. Cheng, Dynamic increase factors of concrete-like materials at very high strain rates, Constr. Build. Mater. **345**, 128270 (2022).
25 X. Zhang, H. Hao, and G. Ma, Dynamic material model of annealed soda-lime glass, Int. J. Impact Eng. **77**, 108 (2015).
26 S. Chocron, C. E. Anderson Jr., K. A. Dannemann, and A. E. Nicholls, Pressure effects on the compressive response of confined intact and damaged soda-lime glass, Exp. Mech. **53**, 77 (2013).
27 H. X. Mei, S. Gowrishankar, K. M. Liechti, and R. Huang, in Initiation and propagation of interfacial delamination in integrated thin-film structures: Proceedings of 2010 12th IEEE Intersociety Conference on Thermal and Thermomechanical Phenomena in Electronic Systems, Las Vegas, 2010.
28 M. L. Benzeggagh, and M. Kenane, Measurement of mixed-mode delamination fracture toughness of unidirectional glass/epoxy composites with mixed-mode bending apparatus, Compos. Sci. Tech. **56**, 439 (1996).
29 D. A. Shockey, A. H. Marchand, S. R. Skaggs, G. E. Cort, M. W. Burkett, and R. Parker, Failure phenomenology of confined ceramic targets and impacting rods, Int. J. Impact Eng. **9**, 263 (1990).
30 H. N. G. Wadley, M. R. O'Masta, K. P. Dharmasena, B. G. Compton, E. A. Gamble, and F. W. Zok, Effect of core topology on projectile penetration in hybrid aluminum/alumina sandwich structures, Int. J. Impact Eng. **62**, 99 (2013).
31 H. Yazdani Sarvestani, M. Mirkhalaf, A. H. Akbarzadeh, D. Backman, M. Genest, and B. Ashrafi, Multilayered architectured ceramic panels with weak interfaces: Energy absorption and multi-hit capabilities, Mater. Des. **167**, 107627 (2019).
32 Z. Wei, and X. Xu, Gradient design of bio-inspired nacre-like composites for improved impact resistance, Compos. Part B-Eng. **215**, 108830 (2021).
33 Z. Yin, F. Hannard, and F. Barthelat, Impact-resistant nacre-like transparent materials, Science **364**, 1260 (2019).
34 X. Zhang, K. Wu, Y. Ni, and L. He, Anomalous inapplicability of nacre-like architectures as impact-resistant templates in a wide range of impact velocities, Nat. Commun. **13**, 7719 (2022).
35 K. Wu, Z. Zheng, S. Zhang, L. He, H. Yao, X. Gong, and Y. Ni, Interfacial strength-controlled energy dissipation mechanism and optimiza-

tion in impact-resistant nacreous structure, Mater. Des. **163**, 107532 (2019).
36 M. J. Forrestal, and V. K. Luk, Dynamic spherical cavity-expansion in a compressible elastic-plastic solid, J. Appl. Mech. **55**, 275 (1988).
37 M. J. Forrestal, and D. Y. Tzou, A spherical cavity-expansion penetration model for concrete targets, Int. J. Solids Struct. **34**, 4127 (1997).

仿贝壳结构在低/高速冲击载荷下的能量吸收和失效机理: 数值模拟研究

高伟韬, 王子豪, 彭克锋, 王克鸿, 周琦, 郑志军

摘要 仿贝壳结构在低速冲击下表现出优秀的力学性能, 但其在高速冲击下的有效性尚不明确. 在本研究中, 我们使用有限元方法模拟了球形弹丸在较大速度范围内冲击仿贝壳板的过程. 构建了一个三维有限元模型, 并根据靶板穿孔测试中残余速度和断裂形态验证了其有效性. 系统地研究了冲击速度、界面强度和几何尺寸对抗冲击性能的影响, 并提出了一个无量纲的几何参数来揭示影响结构断裂韧性的机制. 研究发现, 随着冲击速度的增加, 珍珠层材料的抗冲击性能逐渐减弱; 在高速冲击下, 其抗冲击性能弱于均质板. 此外, 仿贝壳结构的断裂韧性取决于不同冲击速度下“界面增强”与“强度削弱”之间的竞争机制. 这些发现为生物启发结构应用于防护材料设计提供了重要的指导.